



# Effect of Microstructural Characteristics on Mechanical Properties of Ferritic Stainless Steel

Mitsuhiro Okayasu and Tomoki Shigeoka

(Submitted June 13, 2019; in revised form October 19, 2019; published online November 1, 2019)

To improve the mechanical properties of hot-rolled ferritic stainless steel (SUS430), the microstructural characteristics of SUS430 were changed using a heating process under various conditions. The hardness of SUS430 decreased upon the increase in the heating temperature to 900 °C, and the hardness increased when the sample was heated to temperatures greater than 900 °C. The high hardness of the sample heated at 1000 °C ( $H_{1000\text{ °C}}$ ) is attributed to the heating time: A high hardness was obtained for a  $H_{1000\text{ °C}}$  sample that was heated for 1 h ( $H_{1000\text{ °C-1h}}$ ), but this decreased when the heating time was increased to more than 1 h. The high hardness of  $H_{1000\text{ °C-1h}}$  is caused by the fine  $\text{Cr}_{23}\text{C}_6$  precipitates that are distributed in the sample around the grain boundaries. On the other hand, the large precipitates of  $\text{Cr}_{23}\text{C}_6$  in  $H_{1000\text{ °C-12h}}$  decrease the hardness. The hardness value of SUS430 is directly attributed to the mechanical properties and the ultimate tensile strength. The tensile strength of  $H_{1000\text{ °C-1h}}$  was found to be about 200% and 20% higher than the as-received and  $H_{1000\text{ °C-12h}}$  samples, respectively. Despite the increase in the tensile strength of the  $H_{1000\text{ °C-1h}}$  sample, the ductility was not found to decrease significantly, for example, the fracture strain was approximately 25%. This occurrence is affected by a severe slip in the ferrite base grain, and the high strength of  $H_{1000\text{ °C-1h}}$  is influenced by the interruption of the slip by the  $\text{Cr}_{23}\text{C}_6$  precipitates. Unlike the tensile strength, similar fatigue properties were observed for both  $H_{1000\text{ °C-1h}}$  and  $H_{1000\text{ °C-12h}}$ , which is associated with the low crack driving force of  $H_{1000\text{ °C-12h}}$ , caused by the roughness-induced crack closure arising from the large  $\text{Cr}_{23}\text{C}_6$  precipitates.

**Keywords** ferrite, heating, mechanical property, precipitation, stainless steel

## 1. Introduction

There are several different types of ferritic stainless steels that are employed in various engineering applications, for example, they are used in boiler tubes, blades and turbine rotors that are used at high temperatures of up to 650 °C (Ref 1). Ferritic stainless steels have a high thermal conductivity and a low thermal expansion coefficient (Ref 2), which are superior to those found in other stainless steels, such as austenite and martensite stainless steels. Ferritic stainless steels are also considered to possess good weldability and a high thermal fatigue performance. Low-chromium ferritics can fall into outer gamma loop ( $\delta + \gamma$ ) which allow the phase structure to be dual phased, with the majority being ferrite and austenite. SUS430 is one of the major ferritic stainless steels, consisting of 16–18 Cr and 0.12 C. Although the ferritic stainless steels have excellent material properties, the material strength and ductility are lower than those found in other stainless steels. To improve the mechanical properties of stainless steels using work and precipitation hardening, various approaches have been employed, including the addition of chemical elements, heat

treatment, severe deformation and surface treatments. Several investigators have examined the mechanical properties of ferritic stainless steel fabricated using the equal channel angular extrusion (ECAE) process at different temperatures, in which a total strain of 2.3 is applied to the ferritic stainless steel (Ref 3). Using the ECAE process, a high ultimate tensile strength of 783 MPa is obtained, which is more than 1.4 times higher than that obtained for the as-received samples. Recently, the mechanical properties of ferritic stainless steels were investigated after a friction stir welding process (Ref 4). Owing to the rapid cooling used in the friction stir welding process, the coarse ferrite grains were altered to become fine grains with a duplex structure of ferrite and martensite. Examination of the microstructural characteristics revealed an acceptable ductility and impact toughness. On the other hand, surface coating using physical vapor deposition (PVD) was carried out on the surface of ferritic stainless steel, and this process led to a high hardness and corrosion resistance (Ref 5).

The mechanical properties of ferritic stainless steel with 38 Cr have been further investigated after aging at 475 °C. Physical changes were found to occur, in the toughness and hardness in particular, owing to the aging process and the  $\alpha \rightarrow \alpha\text{Fe} + \alpha''_{\text{Cr}}$  spinodal decomposition reaction (Ref 6). After the aging process, the hardness value increased toward twinning during the deformation. On the other hand, a rapid deterioration in the toughness occurs at 475 °C, which is affected by the pinning of the dislocations. The effect of Nb on the high-temperature strength was studied in ferritic stainless steel (Ref 7), and an increase in the high-temperature proof strength occurred upon addition of Nb at 700 °C for 2 h, and fine  $\text{Fe}_2\text{Nb}$  Laves phase particles with a diameter of 0.02  $\mu\text{m}$  were obtained. Furthermore, an extremely strong diffraction peak for Nb(C,N) was obtained, although a weak diffraction

Mitsuhiro Okayasu and Tomoki Shigeoka, Graduate School of Natural Science and Technology, Okayama University, 3-1-1 Tsushimanaka, Kita-ku, Okayama 700-8530, Japan. Contact e-mail: mitsuhiro.okayasu@utoronto.ca.

peak for  $M_6C$  was detected. The embrittlement characteristics of ferritic stainless steels were examined by Grobner (Ref 8), who reported that a decrease in the room temperature toughness is observed after exposure to a temperature of 538 °C for about 1000 h; this decrease in the toughness is attributed to the precipitation of the carbonitrides. Based on previous studies, it is proposed that the mechanical properties of ferritic stainless steels can be improved by modification of the microstructure during the heating processes. As previously reported experimental approaches have mainly been conducted at a heating temperature of less than 550 °C, an examination of the material properties of ferritic stainless steels after heating to high temperatures is required. The microstructural characteristics of ferritic stainless steels can be altered significantly at high temperatures of around 1000 °C, that is,  $\gamma$  phase transformation. This occurrence might improve the mechanical properties of the related stainless steels. Thus, in the present work, the mechanical properties of SUS430 were examined experimentally after heating to temperatures greater than 800 °C.

## 2. Experimental Procedures

### 2.1 Material Preparation

Several hot-rolled ferritic stainless steel sheets (SUS430) were used in this study; they were supplied by Nippon Steel & Sumikin Stainless Steel Corp, Japan. The thickness of the stainless steel sheet was about 6.5 mm, and the chemical composition of SUS430 is listed in Table 1. To examine the effect of the microstructural characteristics on the mechanical properties, the SUS430 sheet was heated at various temperatures (830–1000 °C) and times (0.5–12 h). The recrystallization temperatures of the appropriate stainless steels were used as the basis for determining the experimental temperatures used (Ref 9).

The mechanical properties of SUS430 were investigated experimentally, and the hardness, tensile strength and fatigue tests were conducted using a rectangular dumbbell-shaped specimen of  $5.5 \times 1.5 \times 1$  mm. The tensile tests were performed using a screw-driven universal testing machine with a capacity of 50 kN, in which the specimen was loaded at a rate of 1 mm/min until final failure was achieved. The tensile strength and fracture strain were measured using a commercial load cell and strain gauge, respectively.

The fatigue properties were examined using the stress amplitude ( $S_a$ ) and the cyclic number to failure ( $N_f$ ) ( $S_a$ - $N_f$  curves). Cyclic loading was applied to the rectangular-shaped specimen using a sinusoidal wave form at a frequency of 30 Hz and a stress ratio of 0.1, for up to  $10^7$  cycles, that is, the endurance limit. The maximum loading stress was determined based on the ultimate tensile strength, for example, 40–95% of  $\sigma_{UTS}$ .

Electron backscatter diffraction analysis (EBSD) was used to clarify the microstructure, strain and failure characteristics

using a scanning electron microscope (SEM) under the following conditions: an accelerating voltage of 15 kV, a beam current of 12 nA and a step size of 1.7  $\mu$ m. In this analysis, the sample surfaces were polished mechanically using a cloth containing alumina particles.

## 3. Results and Discussion

### 3.1 Microstructural Characteristics

Figure 1 shows the EBSD crystal orientation map (IPF: inverse pole figure) maps for the ferritic stainless steels under various conditions, such as at 830, 850, 900 and 1000 °C for 1 and 12 h. The color levels of each pixel in the IPF maps were determined according to the deviation of the crystal orientation. A severely extruded microstructural formation was easily observed for the as-received (AR),  $H_{830\text{ }^\circ\text{C-12h}}$  and  $H_{850\text{ }^\circ\text{C-12h}}$  samples. On the other hand, grain growth with precipitates was observed for the  $H_{900\text{ }^\circ\text{C-12h}}$  and  $H_{1000\text{ }^\circ\text{C-12h}}$  samples, in which the mean width of the grown grains for both samples is more than 100  $\mu$ m, which is about 20% wider than that for the others. The extent of precipitation was also different, that is, the higher the heating temperature, the stronger the precipitation. Even though grain growth was not clearly observed for  $H_{1000\text{ }^\circ\text{C-1h}}$ , a large amount of fine precipitates were uniformly generated, compared to that for  $H_{1000\text{ }^\circ\text{C-12h}}$ . These precipitates were detected in the sample surrounding the grain boundaries. In this case, the transformation products of  $\gamma$  are associated with ferrite and chromium carbide,  $Cr_{23}C_6$  (Ref 10). Figure 1 also shows the SEM image showing the  $Cr_{23}C_6$  and the result of its XRD analysis. In a previous study published by Huang et al. (Ref 11), a similar examination was performed and precipitates of  $Cr_{23}C_6$  were obtained. Westbrook reported that the hardness of  $Cr_{23}C_6$  measured is as high as about 6.37 GPa (Vickers hardness) (Ref 12). A change in the microstructural characteristics could give different mechanical properties. It should be noted that the corrosion resistance of the ferritic stainless steels is affected by the resistance of the oxide film when it is heated to high temperatures of over 1000 °C (Ref 13). Based on this information, a study of the corrosion characteristics of SUS430 after heating to high temperatures should be performed in the future.

### 3.2 Mechanical Properties

Figure 2 shows the Vickers hardness of the stainless steels with and without the heating processes. A considerable drop in the hardness value is clearly observed as the samples are heated at 830 and 850 °C, and this drop is observed even after a short period of heating, for example, 0.5 h. On the other hand, the hardness value decreased linearly with an increase in the heating time of up to 1 h for the  $H_{900\text{ }^\circ\text{C}}$  sample, at which the hardness value became saturated. In contrast, a variation in the hardness was obtained for the  $H_{1000\text{ }^\circ\text{C}}$  sample. As observed,

**Table 1 Chemical composition of ferritic stainless steel (in wt.%)**

	C	Si	Mn	P	S	Ni	Cr	Mo	N
SUS430	0.058	0.41	0.26	0.026	0.002	0.10	16.2	0.05	0.03

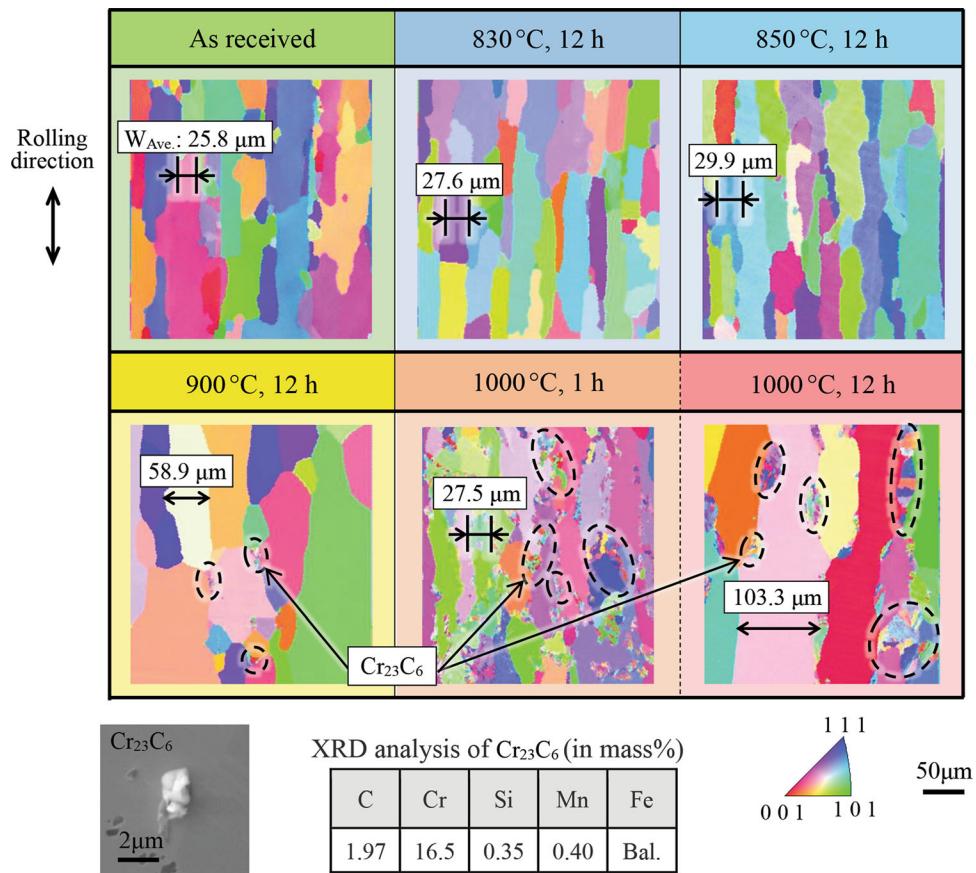


**Fig. 1** Inverse pole figure (IPF) maps for the ferritic stainless steel samples and Cr<sub>23</sub>C<sub>6</sub> precipitates with and without regulated microstructures

the hardness of the H<sub>1000 °C</sub> sample was enhanced by an increase in the heating time of up to 1 h, and this drops as it is heated to 12 h. To verify the mechanical properties, tensile tests were carried out.

Figure 3 shows the representative engineering tensile stress versus strain (*S*–*S*) curves for the as-received and heated samples, and based on the *S*–*S* curves, the tensile properties are summarized in Fig. 4. The tensile properties were observed to differ depending on the sample. A tensile strength ( $\sigma_{UTS}$ ) increased with increasing the heating temperature to 1000 °C, although the  $\sigma_{UTS}$  value for H<sub>1000 °C-1h</sub> is about 100 MPa higher than that for H<sub>1000 °C-12h</sub>. For the duration of 1 h, the high tensile strength was affected by the widely distributed tiny Cr<sub>23</sub>C<sub>6</sub> precipitates, as described above. As the high tensile strength was obtained for the H<sub>1000 °C-1h</sub> samples, its strain value ( $\epsilon_f$ ) was lower than that for H<sub>1000 °C-12h</sub>, which is similar that for AR one. In this instance, the  $\sigma_{UTS}$  for H<sub>1000 °C-1h</sub> was about 200% higher compared to that obtained for the AR sample, and the  $\epsilon_f$  for H<sub>1000 °C-1h</sub> was only 20% lower than that found for the AR sample. The reason behind this is discussed in a later section of this paper. On the other hand, the tensile strength of the AR sample was higher than that observed in the H<sub>850-12h</sub> sample, which is due to the severe internal strain that is caused by the rolling process in the AR sample. This occurrence can be verified using the *S*–*S* curves, as a high yield strength, as well as a low work-hardening rate, was observed for the AR sample compared to those obtained for the H<sub>850 °C-12h</sub> sample, as indicated in Fig. 3. It is also clear that the obtained tensile strength for the four samples can be relatively correlated with their hardness values, for AR sample, as shown

in Fig. 2, for example,  $\sigma_{UTS}$  (MPa) = 201.7 × HV (GPa),  $R^2 = 0.5$ . It should be noted that the obtained equation could be altered as the size of specimen and loading condition are changed.

The fatigue properties were also investigated, and the obtained  $S_a$ – $N_f$  curves for the representative samples (AR, H<sub>850 °C-12h</sub>, H<sub>1000 °C-1h</sub> and H<sub>1000 °C-12h</sub>) are displayed in Fig. 5. It should be noted that the arrows shown in this figure indicate the test specimens that did not fail within 10<sup>7</sup> cycles. The results obtained are similar to those observed for the tensile strength; a high fatigue strength was detected for the samples that were heated at 1000 °C. However, despite the low tensile strength obtained for H<sub>1000 °C-12h</sub> compared to that for H<sub>1000 °C-1h</sub>, the endurance limit ( $\sigma_1$ ) at 10<sup>7</sup> cycles was observed to be similar or slight high for H<sub>1000 °C-12h</sub>, that is, about 140 MPa. Interestingly, a slightly higher fatigue strength was obtained at a lower stress amplitude for H<sub>1000 °C-12h</sub> compared to that obtained for H<sub>1000 °C-1h</sub>, although the opposite trend was seen for the applied high stress amplitude, that is, the  $S_a$ – $N_f$  curve of H<sub>1000 °C-12h</sub> was crossed with that of H<sub>1000 °C-1h</sub> at about 5 × 10<sup>5</sup> cycles. A similar experimental result was obtained by Bandara and Siriwardance in their previously published study (Ref 14). In this case, a different trend for the  $S_a$ – $N_f$  curve was observed and this was found to be affected by different failure characteristics, which will be discussed in a later section of this paper. The mean endurance limit ( $\sigma_1$ ) for both the H<sub>1000 °C</sub> samples (about 140 MPa) was more than 20% higher compared to those obtained for the other samples. It should be pointed out that the endurance limits for our samples are all lower levels, i.e., the slope of the  $S_a$ – $N_f$  curves is

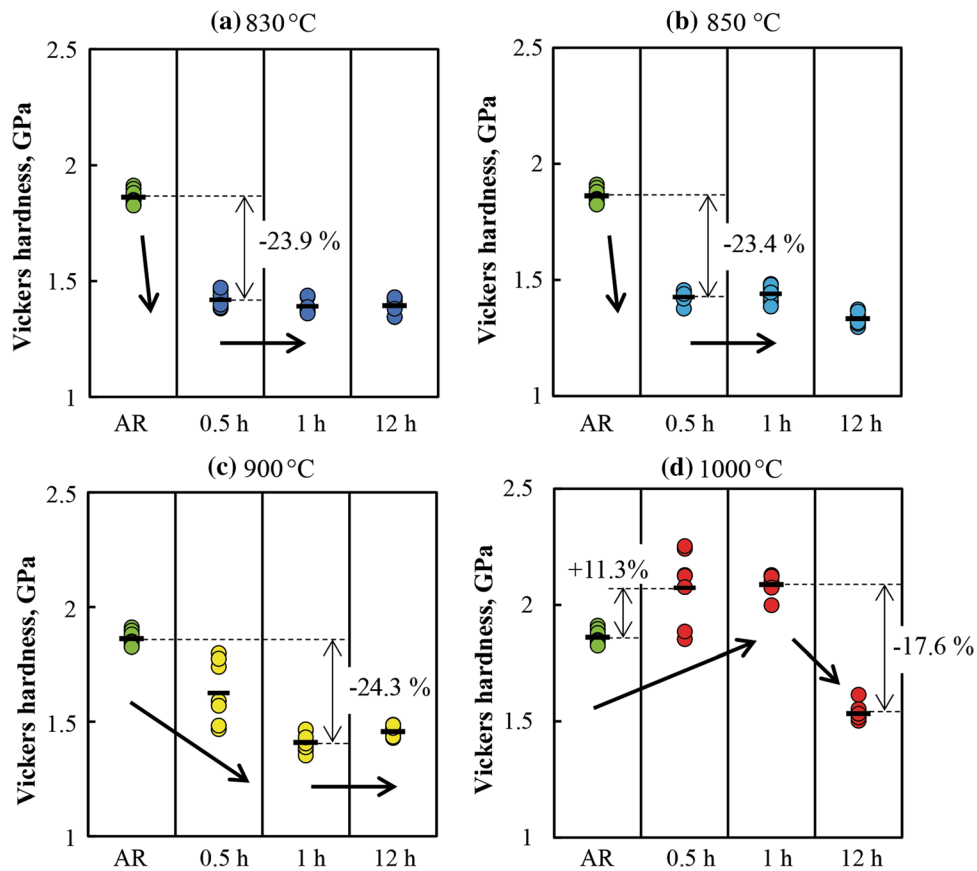


**Fig. 2** Variation in the Vickers hardness of the ferritic stainless steel samples with and without microstructural regulation: (a) 830 °C, (b) 850 °C, (c) 900 °C and (d) 1000 °C

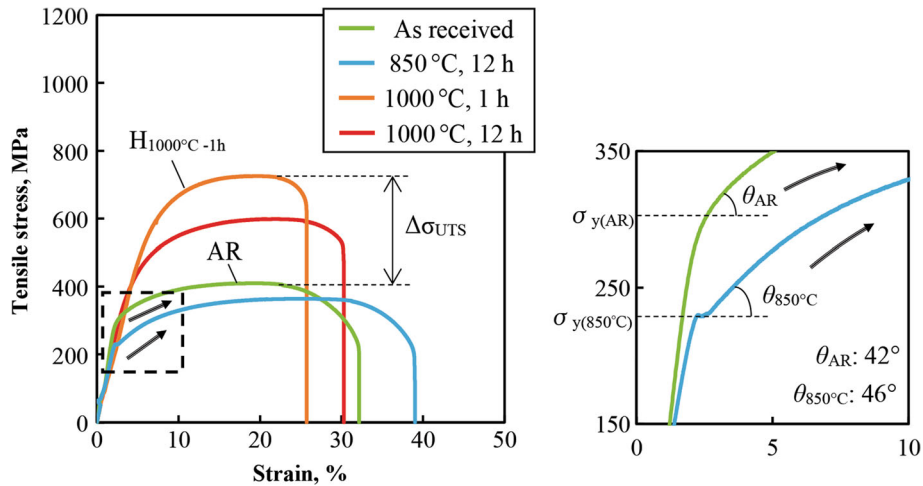


**Fig. 3** Engineering tensile stress–strain curves and their tensile properties for the as-received and heated ferritic stainless steel samples ( $H_{850\text{ °C-12h}}$ ,  $H_{1000\text{ °C-1h}}$  and  $H_{1000\text{ °C-12h}}$ )

high level. Such reduction of endurance limit for stainless steel is observed in Ref. 15, which is attributed to the extent of residual stress of the sample. It is reported that the fatigue strength could be correlated with the distribution and location of the fatigue fracture nucleation sites; the data plots in  $S_a-N_f$  curves (Fig. 5) might be attributed to our sample conditions, such as internal stress and surface roughness (Ref 15).

The solid curves for the  $S_a-N_f$  relationship can be evaluated using a power law dependence with the following formula:  $S_a = \sigma_f N_f^b$ , MPa, where  $\sigma_f$  is the fatigue strength coefficient,  $N_f$  is the cycle number to final fracture and  $b$  is the fatigue exponent. In this case, a high fatigue strength was expected to give an increasing fatigue strength coefficient ( $\sigma_f$ ) and a decreasing fatigue exponent ( $b$ ). The values of  $\sigma_f$  and  $b$  for both  $H_{1000\text{ °C}}$  samples, obtained using least squares analysis, were

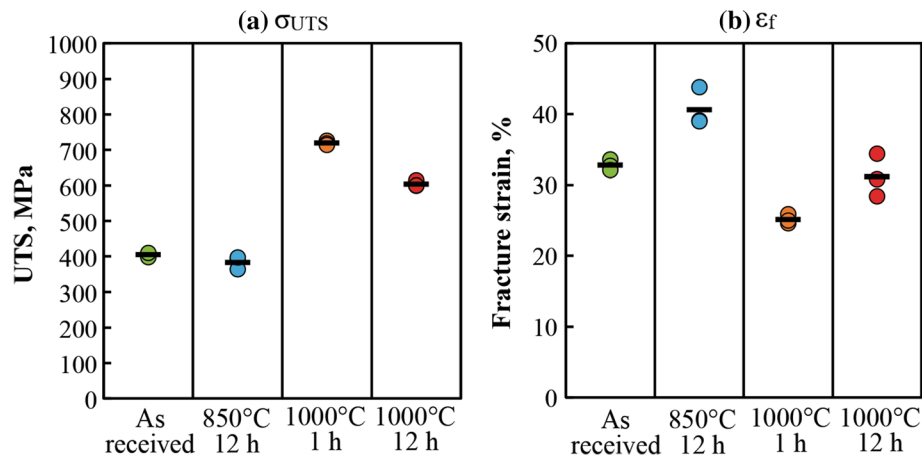


**Fig. 4** Results of the tensile stress and strain for the as-received and heated ferritic stainless steel samples ( $H_{850\text{ }^{\circ}\text{C-12h}}$ ,  $H_{1000\text{ }^{\circ}\text{C-1h}}$  and  $H_{1000\text{ }^{\circ}\text{C-12h}}$ ): (a) ultimate tensile strength (UTS) and (b) fracture strain

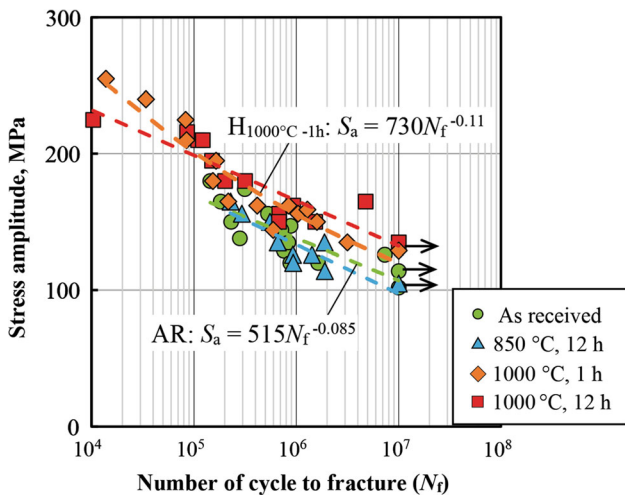


**Fig. 5** Stress amplitude vs. cyclic number to failure ( $S_a-N_f$ ) for the as-received and heated ferritic stainless steel samples ( $H_{850\text{ }^{\circ}\text{C-12h}}$ ,  $H_{1000\text{ }^{\circ}\text{C-1h}}$  and  $H_{1000\text{ }^{\circ}\text{C-12h}}$ )

about  $\sigma_f = 730$  MPa and  $b = -0.11$ . In contrast, lower fatigue properties were also estimated for both the  $H_{850\text{ }^{\circ}\text{C-12h}}$  and AR samples:  $\sigma_f = 515$  MPa and  $b = -0.085$ . The value of  $\sigma_f$  for the hot-rolled sample (AR) was found to be in fairly good agreement with that obtained for the related hot-rolled low carbon steel,  $\sigma_f = 538$  MPa (Ref 16). From the obtained mechanical properties of our stainless steel samples, it was demonstrated that the mechanical properties of SUS430 can be improved by high-temperature heating owing to the  $\text{Cr}_{23}\text{C}_6$  precipitates.

In the previous work, it has been reported that there is a relatively good linear least squares fits for the fatigue strength coefficient data with the Brinell hardness (HB):  $\sigma_f = 4.25 \text{ HB} + 225$  (MPa) (Ref 17). The HV was examined in the present work (Fig. 2), and the hardness value was converted to the Brinell hardness value using the formula:  $\text{HB} = 0.94 \text{ HV}$ , for example, 143 HB for  $H_{1000\text{ }^{\circ}\text{C-12h}}$ . From the Brinell hardness value, the fatigue strength coefficient can be assessed and was found to be  $\sigma_f = 832.8$  MPa, which is relatively close to that obtained from the  $S_a-N_f$  relationship, which was  $\sigma_f = 730$  MPa.

### 3.3 Failure Mechanism

Figure 6 shows the SEM images and the IPF and kernel average misorientation (KAM) maps for the AR,  $H_{850\text{ }^{\circ}\text{C-12h}}$ ,  $H_{1000\text{ }^{\circ}\text{C-1h}}$  and  $H_{1000\text{ }^{\circ}\text{C-12h}}$  samples after monotonic loading to final failure. Note that KAM value is defined by the mean misorientations between the center point of the kernel and all surrounding points in the kernel, i.e., the local misorientation value of the center point. In this case, the low and high strain regions are displayed with the blue and red color, respectively. Examination of the fracture surfaces in the tensile specimens revealed differences in the fracture behavior. As shown in Fig. 6(a), the dimple and slip base ductile failures are a dominating feature in the AR and  $H_{850\text{ }^{\circ}\text{C-12h}}$  samples. It is evident from the KAM maps for the AR and  $H_{850\text{ }^{\circ}\text{C-12h}}$  samples shown in Fig. 6(b) that a high strain is observed, generated around the crack surface, and the specimens were necked severely as indicated by the arrows. On the other hand, a rugged failure mode is seen in addition to the dimple failure for both the  $H_{1000\text{ }^{\circ}\text{C-1h}}$  and  $H_{1000\text{ }^{\circ}\text{C-12h}}$  samples, in which less slip and weak necking occur. From the KAM maps of both of the  $H_{1000\text{ }^{\circ}\text{C}}$  samples, the extent of the internal strain was found to be lower than that obtained for the other samples.

To understand the strain characteristics in detail, the IPF and KAM maps for  $H_{850\text{ }^{\circ}\text{C-12h}}$  and  $H_{1000\text{ }^{\circ}\text{C-12h}}$  were enlarged and are displayed in Fig. 7. A high internal strain with a slip deformation can be observed which originates from the extruded laminar grain in the  $H_{850\text{ }^{\circ}\text{C-12h}}$  sample, although the extruded microstructural formation has collapsed creating a large number of colonies in the  $H_{1000\text{ }^{\circ}\text{C-12h}}$  sample. The later microstructural formation is caused by severe deformation in the grains with interruption from the slip with the  $\text{Cr}_{23}\text{C}_6$  precipitates. This occurrence infers the relatively high strain and high strength of the  $H_{1000\text{ }^{\circ}\text{C}}$  samples.

Figure 8 shows the fracture surfaces and crack growth characteristics of the four samples (AR,  $H_{850\text{ }^{\circ}\text{C-12h}}$ ,  $H_{1000\text{ }^{\circ}\text{C-1h}}$  and  $H_{1000\text{ }^{\circ}\text{C-12h}}$ ) after the fatigue test. At low magnification, two fracture modes can be distinguished, as indicated by the dashed line, which corresponds to fatigue crack propagation (C) and a final fracture (F). In the fatigue crack growth region, striation-like formations with serrations and a stepped morphology can be detected in the AR and  $H_{850\text{ }^{\circ}\text{C-12h}}$  samples, although a meandering crack is observed for both of the  $H_{1000\text{ }^{\circ}\text{C}}$  samples, which is caused by severe crack growth

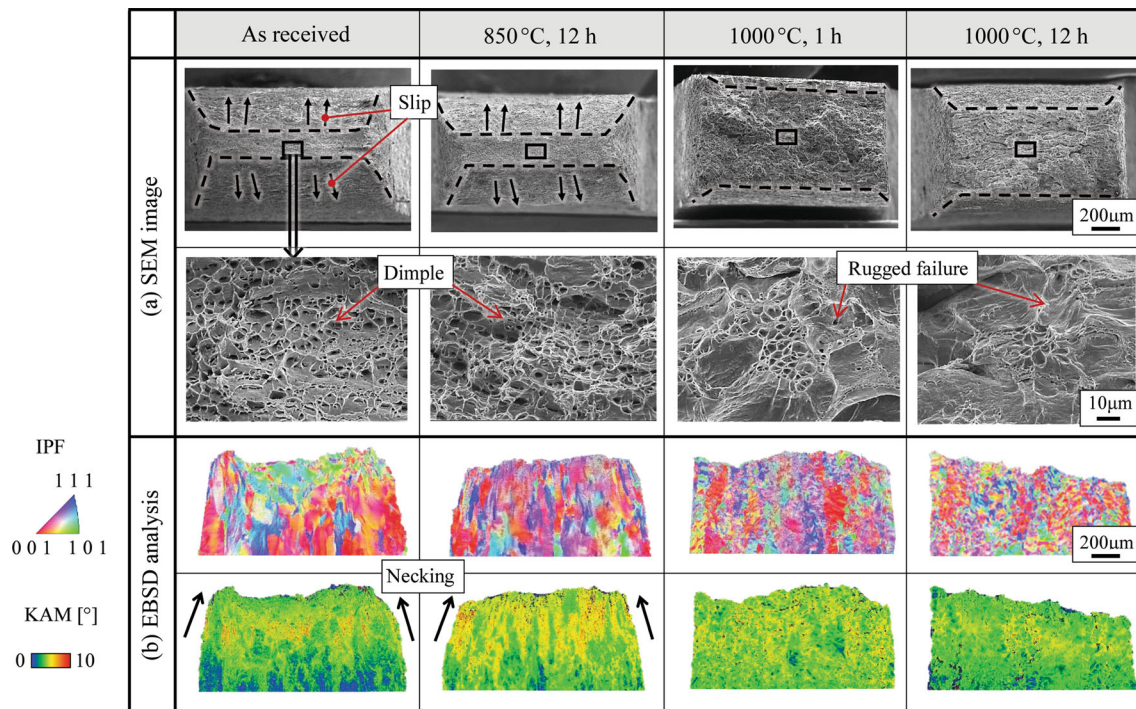


**Fig. 6** Failure characteristics of fracture surfaces of the ferritic stainless steel samples after the tensile test: (a) SEM image and (b) EBSD analysis

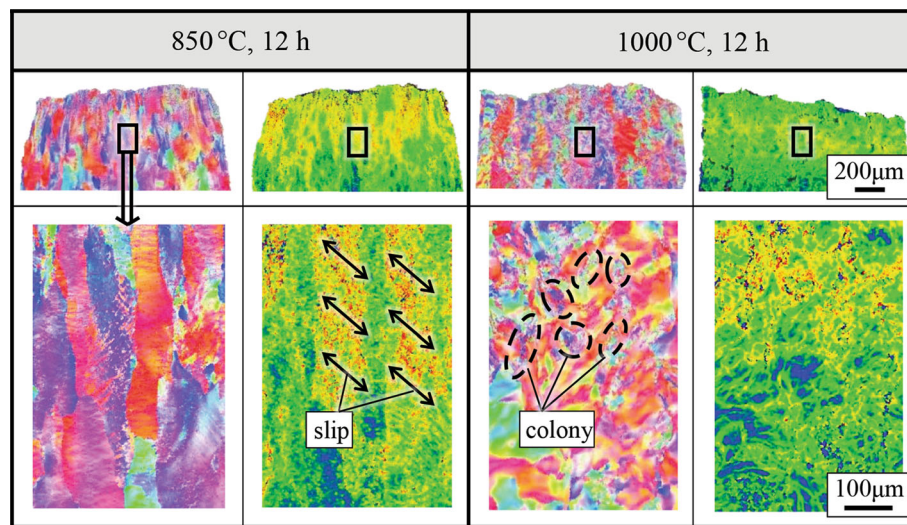


**Fig. 7** IPF and KAM maps of the H<sub>850 °C-12h</sub> and H<sub>1000 °C-12h</sub> samples after the tensile test showing the strain characteristics

resistance arising from the Cr<sub>23</sub>C<sub>6</sub> precipitates. At the final fracture site, slip and rugged base failures are seen, which are associated with failure by monotonic loading, as shown in Fig. 8(a). It is also clear that the area of the fatigue crack growth zone (Fig. 8c) is wider for the H<sub>1000 °C</sub> samples, compared to that observed for the AR and the H<sub>850 °C-12h</sub> samples. This is attributed to the high fatigue strength, that is, the high fracture resistance. From the IPF and KAM maps (Fig. 8b) of the four samples adjacent to the fatigue crack, it can be seen that there are regional variations in the strain characteristics. Basically, the strain characteristics observed after the fatigue test are similar for all of the samples. A high and complicated strain distribution, caused by severe plastic

deformation, is seen in the final failure regions (F), in which a disorganized crystal structure is observed in the IPF maps. On the other hand, the reduced internal strain in the fatigue crack growth region is caused by the high loading speed of 30 Hz, which is faster than that found for the dislocation motion. It should be pointed out that a low internal strain was detected in the samples of H<sub>1000 °C</sub> in the final failure regions, as marked by the dashed circles. This could be attributed to the interruption of the slip deformation due to the fine and hard precipitations of Cr<sub>23</sub>C<sub>6</sub> (Ref 18), which enable a high internal strain.

Figure 9 displays the IPF and KAM maps for the H<sub>1000 °C-1h</sub> sample after the fatigue test and shows the crack growth

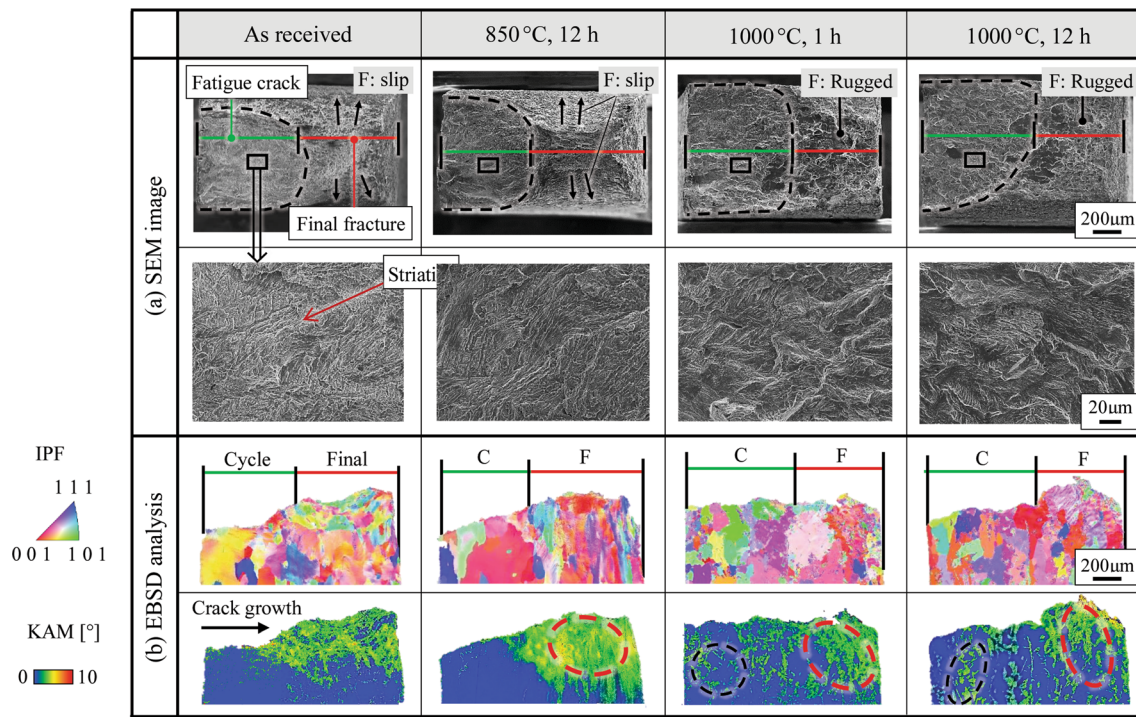


**Fig. 8** Failure characteristics of the fracture surfaces of the ferritic stainless steel samples after the fatigue test: (a) SEM image and (b) EBSD analysis

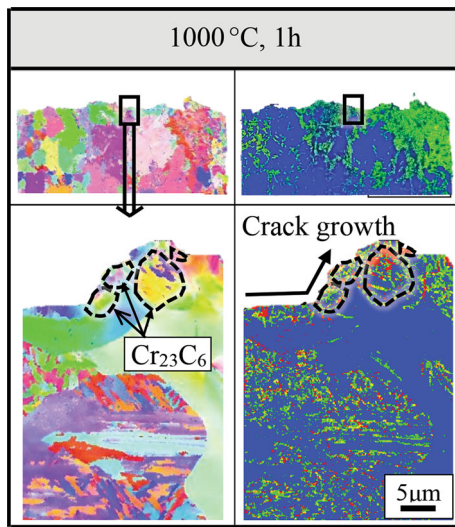


**Fig. 9** IPF and KAM maps of the  $H_{1000\text{ °C-1h}}$  samples adjacent to the fatigue crack

characteristics. It is clear that the crack growth direction is altered, as the crack propagates and reaches the  $Cr_{23}C_6$  precipitates, meaning that meandering crack growth occurs owing to the resistance of the crack path which is caused by the precipitates. The reason for this is attributed to the crack path between the precipitates and ferrite matrix due to their weak bonding strength. This occurrence infers that a rough fatigue crack surface is created in the  $H_{1000\text{ °C}}$  samples, leading to a roughness-induced crack closure. In addition, in ferritic steels, the fracture surface roughness and consequently the crack opening level will increase as the coarseness of the microstructure increases, i.e.,  $H_{1000\text{ °C}}$  samples (Ref 19). As the size of the

$Cr_{23}C_6$  precipitate grows larger in  $H_{1000\text{ °C-12h}}$ , a roughness-induced crack closure could occur compared to that observed in  $H_{1000\text{ °C-1h}}$ , that is, the low crack driving force of  $H_{1000\text{ °C-12h}}$ . This may be especially true, because the  $S_a-N_f$  curve for  $H_{1000\text{ °C-12h}}$  is slight high in the applied low stress amplitude compared to that observed for  $H_{1000\text{ °C-1h}}$ , as shown in Fig. 5, despite the high tensile strength could be obtained for in  $H_{1000\text{ °C-1h}}$ . Therefore, the high fatigue strength of the ferritic stainless steels is affected by the high strength and by severe crack closures.

#### 4. Conclusions

The material properties of SUS430 ferritic stainless steel were experimentally investigated using samples which had different microstructural characteristics. These microstructures were controlled using various heating conditions. The results obtained are summarized as follows:

1. The mechanical properties of ferritic stainless steels are changed by the heating process; this change is dependent on the temperature and heating time. The hardness value of ferritic stainless steel decreases rapidly when it is heated at 830 and 850 °C, and a linearly decreasing hardness is observed when it is heated at 900 °C. On the contrary, the hardness value increases when it is heated at 1000 °C, and an exceptionally high hardness value was obtained for the  $H_{1000\text{ °C-1h}}$  sample.
2. The ultimate tensile strength for the  $H_{1000\text{ °C-1h}}$  sample is about 200% and 12% higher compared to that obtained for the AR and  $H_{1000\text{ °C-12h}}$  samples, respectively. The different tensile properties are attributed to the  $Cr_{23}C_6$

precipitates. Fine Cr<sub>23</sub>C<sub>6</sub> precipitates are observed in the H<sub>1000 °C-1h</sub> sample around the grain boundaries, which results in a high tensile strength. On the contrary, the large Cr<sub>23</sub>C<sub>6</sub> precipitates in the H<sub>1000 °C-12h</sub> sample decrease the tensile strength. On the other hand, no clear Cr<sub>23</sub>C<sub>6</sub> precipitate was observed for the ferritic stainless steel samples that were heated at less than 850 °C. In spite of the high tensile strength of H<sub>1000 °C-1h</sub>, a relatively high material ductility of more than  $\varepsilon_f = 25\%$  was observed.

3. Despite the high tensile strength of H<sub>1000 °C-1h</sub> compared to H<sub>1000 °C-12h</sub>, a similar fatigue strength was obtained, that is, the endurance limit. The reason behind this can be interpreted using the different failure modes, in particular crack closure. The low crack driving force obtained for H<sub>1000 °C-12h</sub> is caused by the severe roughness-induced crack closure arising from the large Cr<sub>23</sub>C<sub>6</sub> precipitates.

## Compliance with Ethical Standards

## Conflict of interest

The authors declare no conflict of interest.

## References

1. T. Fujita, Current Progress Temperature in Advanced High Cr Ferritic Steels for High Applications, *ISIJ Int.*, 1992, **32**, p 175–181
2. S. Patra and L.K. Singhal, Influence of Hot Band Annealing and Cold Rolling on Texture and Ridging of 430 Stainless Steel Containing Aluminum, *Mater. Sci. Appl.*, 2013, **4**, p 70–76
3. N. Saito, M. Mabuchi, M. Nakanishi, I. Shigematsu, G. Yamauchi, and M. Nakamura, Application of Equal Channel Angular Extrusion on Strengthening of Ferritic Stainless Steel, *J. Mater. Sci.*, 2001, **36**, p 3229–3232
4. A.K. Lakshminarayanan and V. Balasubramanian, An Assessment of Microstructure, Hardness, Tensile and Impact Strength of Friction Stir Welded Ferritic Stainless Steel Joints, *Mater. Des.*, 2010, **31**, p 4592–4600
5. C.H. Hsu, C.K. Lin, K.H. Huang, and K.L. Ou, Improvement on Hardness and Corrosion Resistance of Ferritic Stainless Steel via PVD-(Ti, Cr)N Coatings, *Surf. Coat. Technol.*, 2013, **231**, p 380–384
6. M.B. Cortie and H. Pollak, Embrittlement and Aging at 470 °C in an Experimental Ferritic Stainless Steel Containing 38 wt.% Chromium, *Mater. Sci. Eng., A*, 1995, **199**, p 153–163
7. A. Miyazaki, K. Takao, and O. Furukimi, Effect of Nb on The Proof Strength of Ferritic Stainless Steels at Elevated Temperatures, *ISIJ Int.*, 2002, **42**, p 916–920
8. P.J. Grobner, The 885°F (470 °C) Embrittlement of Ferritic Stainless Steels, *Metall. Trans.*, 1973, **4**, p 251–260
9. X. Zhang, Z. Wen, R. Dou, G. Zhou, and Z. Li, Evolution of Microstructure and Mechanical Properties of Cold-Rolled SUS430 Stainless Steel during a Continuous Annealing Process, *Mater. Sci. Eng. A*, 2014, **598**, p 22–27
10. K. Suzuki, S. Asami, and K. Suzuki, Formation of Ridging Related to the Banded Segregation Pattern of Cr and C on Ferritic Stainless Steel Sheet, *Trans. ISIJ*, 1983, **23**, p 731–737
11. X. Huang, D. Wang, and Y. Yang, Effect of Precipitation on Intergranular Corrosion Resistance of 430 Ferritic Stainless Steel, *J. Iron. Steel Res. Int.*, 2015, **22**, p 1062–1068
12. J.H. Westbrook, Temperature Dependence of the Hardness of Secondary Phases Common in Turbine Bucket Alloys, *J. Metal.*, 1957, **209**, p 898–904
13. Y. Yazawa, Y. Kato, and M. Kobayashi, Development of Ti-Bearing High Performance Ferritic Stainless Steels R430XT and RSX-1, *Kawasaki Steel Tech. Rep.*, 1999, **40**, p 23–29
14. C.S. Bandara, S.C. Siriwardane, U.I. Dissanayake, R. Dissanayake, Prediction Methods of Stress Life Curves for Various Stress Ratios for Steels in the High Cycle Region, in *ACEPS-2013*, pp. 75–81
15. N.B. Fredj, M.B. Nasr, A.B. Rhouma, C. Braham, and H. Sidhom, Fatigue life Improvements of the AISI, 304 Stainless Steel Ground Surfaces by Wire Brushing, *ASM Int.*, 2004, **13**, p 564–574
16. A.M. Sherman, Fatigue Properties of Alloy Steels High Strength-Low Alloy Steels, *Metall. Trans. A*, 1975, **6**, p 1035–1040
17. M.L. Roessle and A. Fatemi, Strain-Controlled Fatigue Properties of Steels and Some Simple Approximations, *Int. J. Fatigue*, 2000, **22**, p 495–511
18. A.V. Makarov, E.S. Gorkunov, IYu Malygina, LKh Kogan, R.A. Savrai, and A.L. Osintseva, Eddy-Current Testing of the Hardness, Wear Resistance, and Thickness of Coatings Prepared by Gas-Powder Laser Cladding, *Rus. J. Nondestr. Test.*, 2009, **45**, p 797–805
19. S. Ishihara, Y. Sugai, and A.J. McEvily, On the Distinction Between Plasticity- and Roughness-Induced Fatigue Crack Closure, *Metall. Mater. Trans. A*, 2012, **43A**, p 3086–3096

**Publisher's Note** Springer Nature remains neutral with regard to jurisdictional claims in published maps and institutional affiliations.